Mechanisms of radio frequency modulation reflection spectrum formation of semiconductor heterostructures

© D.V. Protasenya

LLC „VPG Laserone“,
141190 Fryazino, Russia

E-mail: prodim2004@yandex.ru

Received April 2, 2026
Revised June 29, 2026
Accepted August 14, 2026

The paper presents the results of modeling changes in the electron gas parameters of a semiconductor heterostructure consisting of AlGaAs and GaAs layers on a semi-insulating substrate, which was previously studied in the framework of radio frequency modulation reflection experiments. It is demonstrated that when exposed to an external radio frequency field, the value of the formed constant additive to the initial electric field embedded in the heterostructure is insufficient to explain the experimentally obtained change in reflection from the structure of the probing light. An alternative mechanism for changing the reflection coefficient is proposed, based on the direct effect of an alternating field on light reflection, and its correspondence with experimental data is shown. It was demonstrated that in order to observe the radio frequency modulation reflection spectra, the frequency of the electric field must be greater than the inverse relaxation time of free carriers with deep impurities.

Keywords: modulation spectroscopy, semiconductor heterostructure, electron gas kinetics, quantum hydrodynamics, gallium arsenide, two-dimensional electron gas.

DOI: 10.61011/SC.2026.05.63996.9373

1. Introduction

Modulation spectroscopy is one of the principal methods for obtaining information about the properties of semiconductor materials and structures [1]. Its methods can determine critical-point energies, exciton binding energies, internal electric fields, and charge carrier concentrations. The basic principle of modulation spectroscopy is to measure the derivative of the optical reflectance spectrum with respect to a parameter, such as temperature (thermoreflectance [2]) or strain (piezoreflectance [3]). Methods involving electric field modulation, namely electroreflectance [4] and photoreflectance [5], are the most widely used. The latter is preferred because it can be implemented without contact: reflectance is varied by modulating a laser beam. However, photoreflectance has several drawbacks, including a photoluminescence signal that overlaps the signal of interest, an effect that is particularly pronounced at low sample temperatures [5].

This motivates the search for new modulation spectroscopy methods, including radio frequency modulated reflectance (RMR), first proposed in Ref. [6]. This method involves measuring changes in the reflectance of probe radiation from a heterostructure subjected to a radio frequency field at a frequency in the range $1-30$ MHz, which is additionally modulated at a low frequency ($100-300$ Hz). The optical reflectance of the probe radiation is measured at the modulation frequency. To explain the experimental light reflectance spectra obtained in Ref. [6], a mechanism involving an additional contribution to the electric field built into the semiconductor heterostructure was proposed, by analogy with photoreflectance and electroreflectance. The origin of this additional contribution was not specified in Ref. [6]. Charge carrier heating by the radio frequency (RF) field and unequal probabilities of carrier transfer between different heterostructure layers [7] were subsequently proposed as hypotheses. The lack of an unambiguous interpretation of the spectra has prevented RMR from becoming as popular as conventional electroreflectance [8]. To establish the role of the induced contribution to the built-in electric field in the reflected signal and identify its precise mechanism, the effect of the RF field on the sample must be modeled mathematically. Mathematical modeling has, for example, provided an interpretation of electroreflectance spectra [9].

2. Mathematical model

2.1. Experimental configuration

RMR was experimentally observed in a heterostructure with the following layers: a 100 nm $Al_{0.2}Ga_{0.8}As$ layer with a donor concentration of $8 \cdot 10^{17}\,cm^{-3}$, a 500 nm undoped GaAs layer, and a semi-insulating (SI) GaAs substrate [6]. A two-dimensional electron gas forms at the GaAs/AlGaAs interface. The electric field was applied perpendicular to the wafer using planar electrodes (Figure 1). The calculations were based on the experimental data reported in Ref. [6].

2.2. Initial equilibrium

First, the equilibrium charge and field distributions were determined by solving Poisson's equation with the charge taken to be a function of the potential:

$$\nabla(\varepsilon_0 \varepsilon \nabla \varphi) = -\rho(\varphi). \quad (1)$$

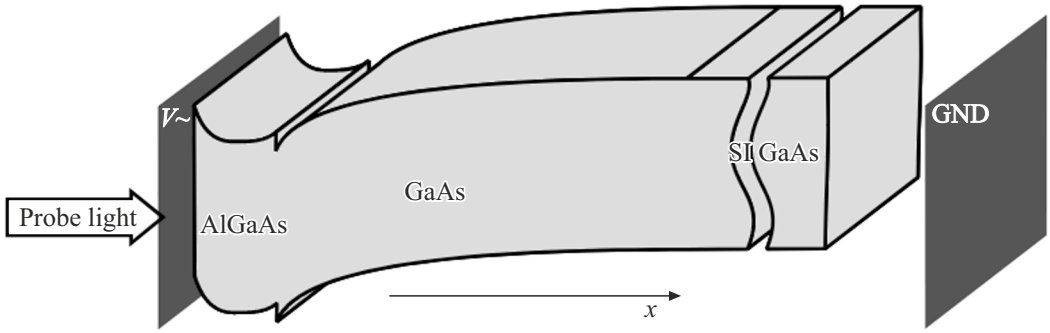


Figure 1. Configuration of the heterostructure studied by RMR.

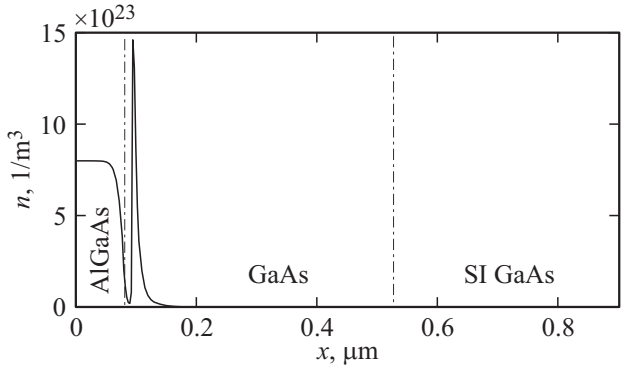


Figure 2. Equilibrium electron concentration distribution.

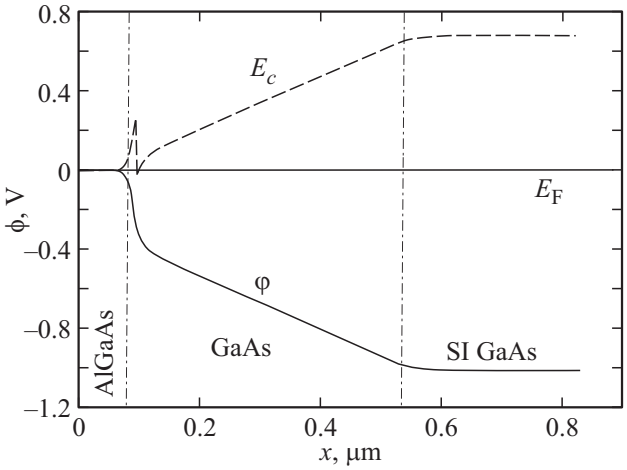


Figure 3. Equilibrium distributions of the potential (ϕ) and conduction band edge (E_c). E_F denotes the Fermi level.

Here φ is the potential, ρ is the charge density, and ε is the relative permittivity of the sample ($\varepsilon = 12$ [10]). The charge in the heavily doped AlGaAs layer and the charge of deep impurities in the substrate were calculated using the Fermi–Dirac distribution, whereas the Boltzmann distribution was used for the GaAs layer. In the two-dimensional electron gas region, the potential and electron concentration can be approximately described using the density-gradient method [11–14]:

$$\frac{2b}{S}\left(\frac{1}{m}\frac{\partial^2 S}{\partial x^2}\right) = \Phi - \varphi + \frac{T}{e}\ln(S^2), \tag{2}$$

where $S = \sqrt{n/n_i}$, $b = \hbar^2/12e$, n_i is the intrinsic electron concentration, n is the electron concentration, m is the electron effective mass, T is the temperature (in energy units), $\hbar$ is the reduced Planck constant, e is the electron charge, and Φ is the potential corresponding to the intrinsic electron concentration in the sample. This equation resembles the Schrödinger equation, with S playing the role of the wave function (its square is proportional to the electron concentration), and enables a classical description of quantum effects (size quantization) in the sample. Equation (2) shows that quantum corrections can be incorporated through an effective contribution

$$\frac{2b}{S}\left(\frac{1}{m}\frac{\partial^2 S}{\partial x^2}\right)$$

to the potential. Numerical iterative solution of the equations yielded the equilibrium electron density distribution (Figure 2) and potential distribution in the sample (Figure 3). The layer boundaries are indicated by dash-dotted lines. The peak at the AlGaAs/GaAs interface corresponds to the formation of a two-dimensional electron gas.

2.3. Free carrier kinetics neglecting impurities

The effect of the external radio frequency field was considered in two stages. In the first stage, the dynamics of the deep impurity charge in the substrate (electron transitions between the conduction band and deep levels) were neglected. This is justified because the field period is shorter than the time for these transitions (the impurity relaxation time) [15]. The electron gas kinetic equations were written in the hydrodynamic approximation [16]:

$$\frac{\partial n}{\partial t} + \frac{\partial n u_j}{\partial x_j} = 0, \tag{3}$$

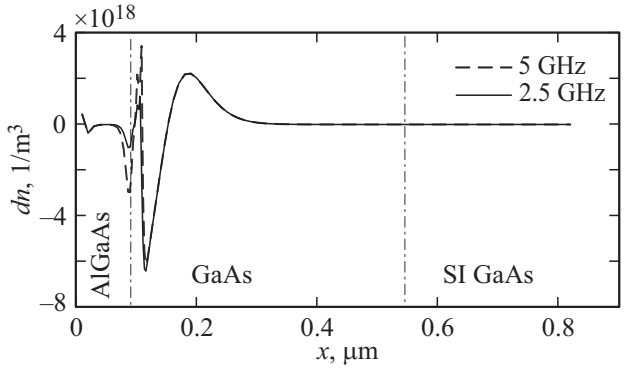


Figure 4. Steady-state distribution of the electron concentration change in the sample, neglecting impurity dynamics.

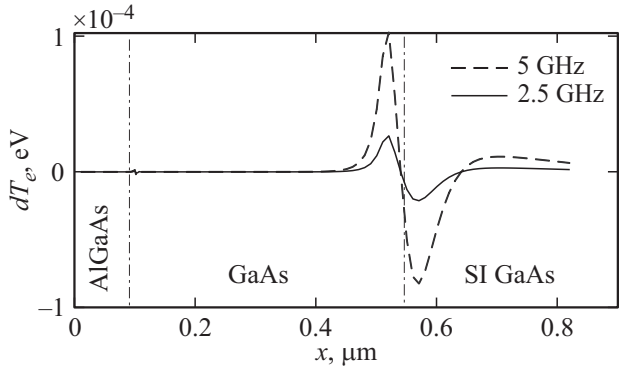


Figure 5. Steady-state distribution of the electron gas temperature change in the sample, neglecting impurity dynamics.

$$\frac{\partial u_j}{\partial t} + u_i \frac{\partial u_j}{\partial x_i} + \frac{1}{mn} \frac{\partial nT_e}{\partial x_j} - \frac{e}{m} \frac{\partial \varphi}{\partial x_j} = -\frac{u_j}{\tau_p}, \qquad (4)$$

$$\frac{\partial T_e}{\partial t} + u_j \frac{\partial T_e}{\partial x_j} + \frac{2}{3} T_e \frac{\partial u_j}{\partial x_j} = -\frac{T_e - T_0}{\tau_e} + \frac{2mu^2}{3\tau_p}, \qquad (5)$$

where u is the velocity, T_e is the electron gas temperature (in energy units), T_0 is the crystal lattice temperature (25 meV), τ_p is the electron momentum relaxation time (0.3 ps), and τ_e is the electron energy relaxation time (1 ps) [17]. These equations must be supplemented by Poisson's equation (1), with boundary conditions determined by the electrode potentials. The field acting on the electrons was assumed to be relatively weak (far from breakdown), allowing the concept of an electron gas temperature to be used. The equations were numerically integrated over several field periods. The field amplitude and frequency were 10 kV/cm [6] and 5 GHz, respectively. The frequency was artificially increased relative to the experimental value to keep the computation time reasonable. The accuracy of the calculations was ensured by solving the equations for perturbations of the initial concentration dn, temperature dT_e, and potential $d\phi$ distributions.

The steady-state distributions $\overline{dn}$ and $\overline{dT_e}$ established by the field were calculated by averaging dn and dT_e over the final field period (Figures 4, 5). Increasing the number of field periods beyond three changes the result only slightly.

When the field frequency is halved (to 2.5 GHz), the steady-state temperature change decreases by a factor of four, while its distribution retains its shape. The steady-state distribution of the electron concentration increment does not change significantly. Thus, electron gas heating and the field frequency have virtually no effect on the final dn distribution, which can therefore be extrapolated to the experimental frequency range (10 MHz). Both dn and dT_e depend quadratically on the field amplitude.

2.4. Slow time scale

To account for impurity dynamics, problem (1), (3)–(5) was solved on two time scales: a fast scale (comparable to the field period and much shorter than the time for the impurity charge to change) and a slow scale (comparable to the time for the impurity charge to change). This approach was used for the pendulum with a vibrating suspension [18]. On the fast time scale, increments in the concentration ($\overline{dn}$) and temperature ($\overline{dT_e}$) of conduction band electrons are generated and maintained (stage 1); on the slow scale, charge is exchanged between the conduction band and impurities (stage 2). To pass to the slow time scale, Eqs. (3)–(5) must be averaged:

$$\frac{\partial dn}{\partial t} = -\frac{\partial n_0 u_j}{\partial x_j} + \frac{\overline{\partial dn}}{\partial t}, \qquad (6)$$

$$\frac{u_j}{\tau_p} = \frac{dn}{mn_0^2} T_e \frac{\partial n_0}{\partial x_j} - \frac{1}{mn_0} T_e \frac{\partial dn}{\partial x_j} - \frac{1}{mn_0} \frac{\partial n_0 dT_e}{\partial x_j} + \frac{e}{m} \frac{\partial d\varphi}{\partial x_j}, \qquad (7)$$

$$dT_e = \overline{dT_e}. \qquad (8)$$

The equations are written in perturbation form, retaining terms of first order in the concentration dn, temperature dT_e, and potential $d\phi$ relative to their initial values (n_0, T_0, φ). The contribution of the fast time scale to the concentration change is represented by $\frac{\overline{\partial dn}}{\partial t}$. The value of $\overline{dT_e}$ was calculated in stage 1. To determine $\frac{\overline{\partial dn}}{\partial t}$, the steady-state distributions calculated in stage 1, $\overline{dn}$, $\overline{dT_e}$, and $\overline{d\varphi}$, must be substituted into (7), and the resulting velocity u_j into (6), with $\frac{\partial dn}{\partial t} = 0$.

To describe deep impurity dynamics, the change in the local Fermi level at some point on the substrate should be considered. A shift by $d\mu$ changes both the impurity charge and the total charge of electrons in the conduction band. These changes are related by

$$dn = dn_D \frac{\partial n}{\partial \mu} \Big/ \left(\frac{\partial n_{a-}}{\partial \mu} - \frac{\partial n_{d+}}{\partial \mu} \right), \qquad (9)$$

where dn_D is the change in the concentration of electrons trapped by impurities, n_{a-} is the concentration of electrons on acceptors, n_{d+} is the concentration of electrons on donors, and μ is the local Fermi level position.

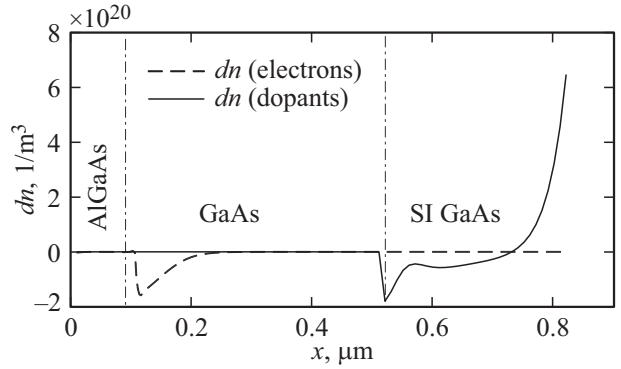


Figure 6. Steady-state distributions of the changes in electron and impurity concentrations, accounting for impurity dynamics.

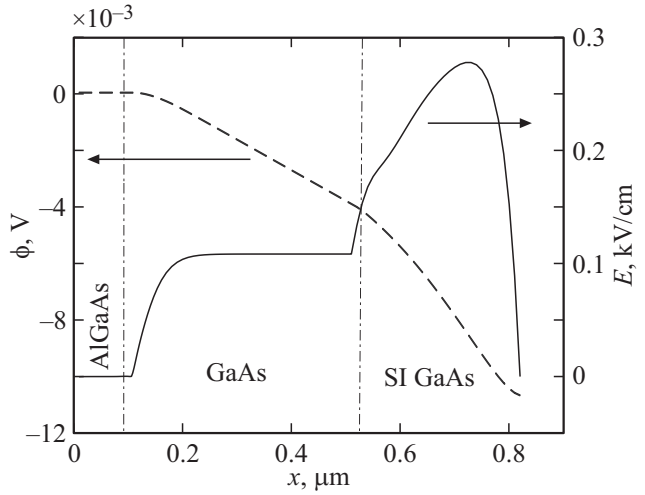


Figure 7. Steady-state distributions of the potential and electric field changes, accounting for impurity dynamics.

This yields the following equations for the charge concentration kinetics:

$$\frac{\partial dn}{\partial t} = -\frac{1}{\tau_{\text{rel}}}\left(dn - dn_D \frac{\frac{\partial n}{\partial \mu}}{\frac{\partial n_{a-}}{\partial \mu} - \frac{\partial n_{d+}}{\partial \mu}}\right), \qquad (10)$$

$$\frac{\partial dn_D}{\partial t} = \frac{1}{\tau_{\text{rel}}}\left(dn - dn_D \frac{\frac{\partial n}{\partial \mu}}{\frac{\partial n_{a-}}{\partial \mu} - \frac{\partial n_{d+}}{\partial \mu}}\right), \qquad (11)$$

where τ_{rel} is the relaxation time. This time is selected during the calculations to ensure convergence, since the final result does not depend on its specific value. Solving the system of Eqs. (1), (6)–(8), (10), (11) yields the steady-state concentration and potential distributions. The results for an external field frequency of 5 GHz are shown in Figure 6. The plot demonstrates electron transfer into the semi-insulating substrate and trapping at impurities. This produces an electric field in the undoped GaAs region, as shown in Figure 7.

3. Estimates of the reflectance change

The field change in the lightly doped region is ~ 0.1 kV/cm, which is clearly insufficient to produce the experimentally observed relative reflectance change of $\Delta R/R \sim 10^{-3}$ reported in Ref. [6]. To verify this, the reflectance change due to the Franz–Keldysh effect must be calculated. This effect provides the main contribution to the reflectance spectrum from regions with a built-in field and is described by

$$\Delta\varepsilon(F) = \frac{A}{(\hbar\omega)^2}\left(\frac{e^2F^2\hbar^2}{2m}\right)^{1/6} H\left(\frac{E_g - \hbar\omega}{\left(\frac{e^2F^2\hbar^2}{2m}\right)^{1/3}}\right), \qquad (12)$$

$$\frac{\Delta R(F, \Delta F)}{R(F)} = \text{Re}\left(e^{2ikx_1} - e^{2ikx_2}\right)\alpha_s\left(\Delta\varepsilon(F + \Delta F) - \Delta\varepsilon(F)\right), \qquad (13)$$

where F and ΔF are the built-in field and its change, α_s is the Seraphin coefficient ($\alpha_s = 0.045$) [19], H is the electro-optic function [20], A is the optical momentum matrix element ($A = 4.43\,\text{eV}^{3/2}$), k is the wave vector ($k = \omega/c\sqrt{\varepsilon}$), x_i are the boundaries of the layer whose contribution is considered, ΔR is the change in the sample reflectance, R is the initial reflectance, ω is the light frequency, and c is the speed of light in vacuum. Subdivision into layers is needed to account for nonuniform built-in fields. The calculations showed that for built-in fields F from 2 to 14 kV/cm, $\Delta R/R$ near the band edge does not exceed 10^{-4}.

Variations of the model parameters (substrate thickness, deep impurity levels, their concentrations, residual impurity concentrations in the undoped region, and relaxation times) do not significantly change the induced built-in field. An alternative mechanism for the formation of the radio frequency modulated reflectance spectrum is therefore needed to explain the RMR results reported in Ref. [6].

4. Alternative spectrum formation mechanism

The electro-optic function H is nonlinear [20]. Consequently, the positive and negative half-cycles of the external electric field contribute differently to reflectance. In particular, an external field with zero mean can change the reflectance spectrum, as described by

$$\frac{\overline{\Delta R(F, \Delta F)}}{R(F)} = \frac{\left(R(F + \Delta F) + R(F - \Delta F) - 2R(F)\right)}{2R(F)}. \qquad (14)$$

Calculations using (14) for built-in fields $F = 1-5$ kV/cm yield nearly an order of magnitude larger values of $\overline{\Delta R}/R$, consistent with experiment. This model can be viewed as rectification of the external field by the nonlinear electro-optic response. Similarly, in layers without a built-in field, excitons affect ΔR, since their contribution is also nonlinear in the electric field. The field changes both the exciton energy and its broadening parameter [21]. The

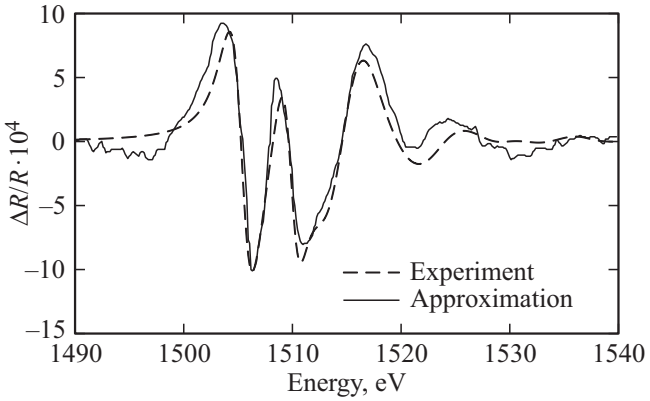


Figure 8. Experimental and fitted RMR spectra.

same applies to layers with a weak built-in field, whose contribution to ΔR upon a field change has the form of a third energy derivative of the dielectric function $\varepsilon(\lambda)$ near a critical point [22]. Experimental electroreflectance spectra are fitted using preliminary information about the heterostructure, yielding refined values of the built-in fields and critical-point energies [23]. Equation (14) was used to fit the RMR spectrum reported in Ref. [6]. The fit to the spectrum measured at 77 K in an external electric field with an amplitude of 5 kV/cm is shown in Figure 8. The exciton energy was taken to be 4 meV, its broadening parameter 1.8 meV, and the broadening parameter for regions with a weak built-in field 1.8 meV; in the strong-field region, the field varied linearly from 1.1 to 3.1 kV/cm.

5. Conventional electroreflectance

The preceding section showed that rectification of the external field by nonlinearities in the response function explains the experimental RMR spectra in Ref. [6], where a voltage source of 10−100 V at 1−30 MHz was used. These voltages are relatively high for such frequencies, raising the question of operation at lower frequencies. The calculations above assumed that the field period did not exceed the relaxation time of deep impurities in the substrate. The opposite case for the same heterostructure, corresponding to conventional electroreflectance, is therefore of interest.

In this case, the calculations must start directly at stage 2. The deep impurities follow all changes in the external field, which can be treated as static. Solving Eqs. (1), (6), (7), (10), (11) yields the electron and impurity charge concentration distributions (Figure 9). Charge accumulates at the sample faces and completely screens the external field. This means that conventional electroreflectance cannot probe samples whose most informative layers lie between a heavily doped surface layer and a semi-insulating substrate. RMR at megahertz frequencies offers a suitable alternative.

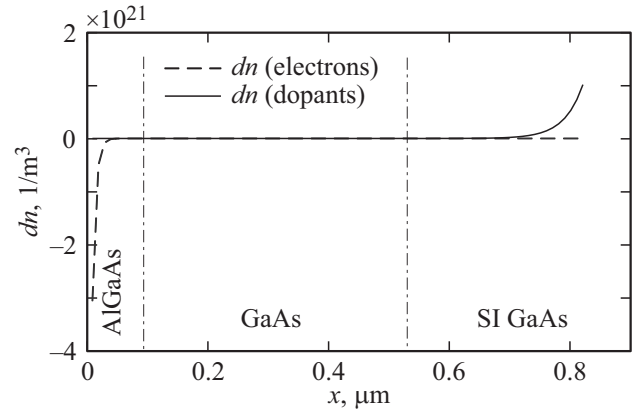


Figure 9. Steady-state distributions of the changes in electron concentrations in the conduction band and on impurities for an electric field period much longer than the impurity relaxation time.

6. Conclusion

A new RMR spectrum formation mechanism has been proposed, based on direct modulation of reflectance by an alternating electric field. Quantitative agreement with measurements has been demonstrated, and an experimental spectrum has been fitted. The increment in the internal heterostructure field induced by an external RF field has been calculated for the first time, and its contribution to the RMR spectrum has been shown to be small. RMR measurements have been demonstrated to probe deeper sample layers than electroreflectance. The electric field period must not exceed the relaxation time of deep impurities in the substrate. The proposed interpretation may encourage use of this method and help it become as widespread as conventional electroreflectance.

Conflict of interest

The author declares that he has no conflict of interest.

References

[1] O.S. Komkov. Phys. Solid State, **63**, 1181 (2021).
[2] D. Pierścińska. J. Phys. D: Appl. Phys., **51**, 013001 (2018). https://doi.org/10.1088/1361-6463/aa9812
[3] D.Y. Lin, Y.S. Huang, Y.F. Chen. Solid State Commun., **107**, 533 (1998). https://doi.org/10.1016/S0038-1098(98)00274-9
[4] X. Yin, Fred H. Pollak. Appl. Phys. Lett., **59**, 2305 (1991). https://doi.org/10.1063/1.106051
[5] D. Saladukha, M.B. Clavel. Phys. Rev. B, **97**, 195304 (2018). https://doi.org/10.1103/PhysRevB.97.195304
[6] O.A. Ryabushkin, V.A. Sablikov. JETP Lett., **67**, 233 (1998). https://doi.org/10.1134/1.567656
[7] A.O. Volkov. *Modulated light reflectance from semiconductor heterostructures under local electromagnetic excitation,* Cand. Sci. Dissertation (Fryazino, IRE RAS, 2001) (In Russian).
[8] O. Ryabushkin, E. Lonskaya. Phys. Status Solidi, **202**, 1282 (2005). https://doi.org/10.1002/pssa.200460906
[9] T. Garcia, V. Deligiannakis. Phys. Status Solidi, **254**, 1700275 (2017). https://doi.org/10.1002/pssb.201700275

[10] O. Madelung. *Semiconductors: Data Handbook,* 3rd ed. (Springer Verlag, Berlin–Heidelberg–N.Y., 2004) p. 123. https://doi.org/10.1007/978-3-642-18865-7
[11] M.G. Ancona, G.J. Iafrate. Phys. Rev. B, **39**, 9536 (1989). https://doi.org/10.1103/PhysRevB.39.9536
[12] M.G. Ancona, H.F. Tiersten. Phys. Rev. B, **35**, 7959 (1987). https://doi.org/10.1103/PhysRevB.35.7959
[13] M.G. Ancona. J. Comput. Electron., **10**, 65 (2011). https://doi.org/10.1007/s10825-011-0356-9
[14] A.R. Brown, A. Martinez, N. Seoane. *Proc. of the 2009 Spanish Conf. on El. Dev.* (Santiago de Compostela, Spain, 2009) p. 140. https://doi.org/10.1109/SCED.2009.4800450
[15] D.C. Look. In: *Semiconductors and Semimetals,* ed. by R.K. Willardson, A.C. Beer (Elsevier, Amsterdam, 1983) v. 19, p. 75.
[16] C.L. Gardner. SIAM J. Appl. Mathematics, **54**, 409 (1994). https://doi.org/10.1137/S0036139992240425
[17] B.P. Zakharchenya, C.V. Shank. *Spectroscopy of nonequilibrium electrons and phonons* (Amsterdam, North-Holland, 1992).
[18] P.L. Kapitza. Usp. Fiz. Nauk, **44**, 7 (1951). https://doi.org/10.3367/UFNr.0044.195105b.0007 (In Russian).
[19] B.O. Seraphin, N. Bottka. Phys. Rev., **145**, 628 (1966). https://doi.org/10.1103/PhysRev.145.628
[20] D.E. Aspnes. Phys. Rev., **153**, 972 (1967). https://doi.org/10.1103/PhysRev.153.972
[21] S. Adachi. Phys. Rev. B, **41**, 1003 (1990). https://doi.org/10.1103/PhysRevB.41.1003
[22] D.E. Aspnes. Surf. Sci., **37**, 418 (1973). https://doi.org/10.1016/0039-6028(73)90337-3
[23] C. Huber, C. Krämmer. Phys. Rev. B, **92**, 075201 (2015). https://doi.org/10.1103/PhysRevB.92.075201